Sub-pixel resolution with color X-ray camera SLcam®

Stanisław H. Nowak,[*a] Aniouar Bjeoumikhov,[ab] Johannes von Borany,[c] Josef Buchriegler,[c] Frans Munnik,[c] Marko Petric,[d] Martin Radtke,[e] Axel D. Renno,[f] Uwe Reinholz,[e] Oliver Scharf,[a] and Reiner Wedell[g]

The color X-ray camera SLcam® is a full-field, single photon detector providing scanning free, energy and spatially resolved X-ray imaging. Spatial resolution is achieved with the use of polycapillary optics guiding X-ray photons from small regions on a sample to distinct energy dispersive pixels on a charged-coupled device detector. Applying sub-pixel resolution, signals from individual capillary channels can be distinguished. Accordingly the SLcam® spatial resolution can be released from pixel size being confined rather to a diameter of individual polycapillary channels. In this work a new approach to sub-pixel resolution algorithm comprising photon events also from the pixel centers is proposed. The details of the employed numerical method and several sub-pixel resolution examples are presented and discussed.

1 Introduction

SLcam® is a high quantum efficiency and throughput color X-ray camera system [1–3] designed for divergent X-ray radiation. It allows detection of single photons with both energy and spatial resolution. SLcam® combines a pn-junction Charged-Coupled Device (pnCCD)[4] with polycapillary optics.[5] The latter can be regarded as a bunch of independent X-ray channels guiding X-ray photons from small regions on a sample to corresponding pixels on pnCCD similarly to the way as fiber optics guide light.

SLcam® employs pnCCD with 48 μm pixel size. Keeping the pixel size fixed spatial resolution of SLcam® can be seriously improved by the use of conically shaped magnifying optics.[2,3] This type of optics is available with magnification factors up to 10:1, allowing representation of 4.8×4.8 μm^2 area in a single pixel. Theoretically, according to Nyquist-Shannon sampling theorem,[6] such a system can correctly resolve details down to ~ 9 μm.

Currently used SLcam® optics are optimized for the pnCCD pixel dimension. The capillary exit diameter is adapted in such a way that the spot size from an individual channel on the detector is approximately equal to the pixel size. However, current technology allows fabrication of polycapillaries with single channel diameter in the range of a micron or even below giving room for further improvement of resolution. Currently pixel size is the limiting factor for spatial resolution of SLcam®.

With the use of a sub-pixel algorithm the dominant role of pixel size can be released. This algorithm divides the signal assigned to each physical pixel over a number of virtual sub-pixels. With such an approach further downscaling of polycapillary channels can be practically used for SLcam® lateral resolution improvement.

Images with sub-pixel resolution are achievable due to specific physics of X-ray photon with Charged-Coupled Device (CCD) interaction that guides to creation of a so-called electron cloud. A non zero area of the cloud leads to charge deposition in pixels nearest to the photon hit. With a correct reconstruction of the footprint of a single photon event the photon hit position can be estimated with a much higher precision than the pixel size.

The sub-pixel resolution algorithm was first applied to Advanced CCD Imaging Spectrometer (ACIS) installed at Chandra X-Ray Observatory (CXO).[7–12] Some years later similar technique was adapted to pnCCD.[13,14] Unfortunately, the proposed routines are neglecting a majority of events analyzing only so-called "corner events", i.e., the photon hits that reach the CCD in proximity to a pixel corner. As a result the sub-pixel image exhibit a grid pattern with the intensity drops in pixel centers.[3] We propose a modified approach taking all the photon hits and distributing them properly over the sub-pixel pattern.

2 Method

2.1 Electron cloud

An X-ray photon absorbed in silicon generates a number of electron-hole pairs amounting to E/W_{Si} – the photon energy E divided by the formation energy of a single electron-hole pair $W_{Si} = 3.6$ eV.[15] In a fully depleted layer the carriers are separated in the vertical electric field and diffuse laterally producing two charge clouds with opposite signs. The holes are col-

lected at the large area cathode. The electrons are transfered to the pixelated anode where they are split over individual pixels. During the readout these charge packets are sequentially transferred to charge amplifiers and counted.

The carrier density of a single photon electron cloud is frequently approximated by a two dimensional Gaussian distribution[11,16–18]:

$$S(x,y) = \frac{Q}{2\pi\sigma_x\sigma_y} \exp\left(-\frac{(x-x_0)^2}{2\sigma_x^2} - \frac{(y-y_0)^2}{2\sigma_y^2}\right), \quad (1)$$

where Q is the total charge produced, σ_x and σ_y are the x and y widths of the cloud, and (x_0, y_0) is the point of a photon hit. For a pixel with coordinates (i, j) the resulting charge intensity I_j^i can be calculated as an integral over a square corresponding to a pixel area:

$$\begin{aligned} I_j^i &= \int_{x_i}^{x_{i+1}} \int_{y_j}^{y_{j+1}} S(x,y)\,dx\,dy = \\ &= \frac{Q}{4}\left(\text{erf}\,\frac{x_{i+1}-x_0}{\sqrt{2}\,\sigma_x} - \text{erf}\,\frac{x_i-x_0}{\sqrt{2}\,\sigma_x}\right) \\ &\quad \cdot\left(\text{erf}\,\frac{y_{j+1}-y_0}{\sqrt{2}\,\sigma_y} - \text{erf}\,\frac{y_j-y_0}{\sqrt{2}\,\sigma_y}\right). \end{aligned} \quad (2)$$

Note that I_j^i is a product of two separable functions depending only on one variable x or y.

Though this is a simplified model neglecting the energy dependence, charge quantization, *etc.*, it shows the fundamental fact making the sub-pixel resolution algorithm possible: on a pixelated plane a single photon electron cloud is normally split over several pixels. For every photon hit, in addition to pixel position, extra information in a form of pixel intensity distribution is gathered. This additional information can be used to determined the center of impact of the photon with sub-pixel accuracy.

2.2 Intensity ratios

A good measure of a single photon electron cloud distribution are the intensity ratios defined as follows:

$$d(I_1, I_2) = \frac{I_2 - I_1}{I_2 + I_1}, \quad (3)$$

where I_1 and I_2 correspond to charge gathered in two different areas of a CCD. Possible values of $d(I_1, I_2)$ ranges from -1 to 1; 0 is reached when $I_1 = I_2$.

It can be shown that for any electron cloud distribution for which x and y components can be separated (*e.g.*, Gaussian distribution) the pixel intensity ratio in x direction is independent from y coordinate and *vice versa*:

$$\begin{aligned} d(I_j^{i-1}, I_j^i) &= d(I_k^{i-1}, I_k^i), \quad \text{and} & (4) \\ d(I_{j-1}^i, I_j^i) &= d(I_{j-1}^l, I_j^l). & (5) \end{aligned}$$

Note also that, provided that for each photon hit the shape of the electron cloud is uniform, the intensity ratio should change monotonically with x and y coordinates of the hit position.

A very elegant way to estimate the single photon electron cloud distribution was presented in Ref 19. The method relies on analysis of a histogram of measured intensity ratios and assumes only a uniform distribution of photon hits over the CCD plane and a Gaussian shape of the charge cloud. The method was used to reveal the size of the cloud. We will use similar methodology to calculate sub-pixel coordinates.

In order to calculate the intensity ratio histogram 2×2 pixel boxes centered at a pixel corner (x_i, y_j) nearest to the point of a photon hit (x_0, y_0) are analyzed; intensity ratios in, respectively, x and y directions are calculated as follows:

$$\begin{aligned} d_x &= d(I_{j-1}^{i-1} + I_j^{i-1},\ I_{j-1}^i + I_j^i) & (6) \\ d_y &= d(I_{j-1}^{i-1} + I_{j-1}^i,\ I_j^{i-1} + I_j^i). & (7) \end{aligned}$$

The intensity ratios in x or y direction computed for all the single photon hits are combined in one histogram.

The histogram normalized to occupy a unitary area can be regarded as an estimation of the probability density function. Accordingly, a normalized intensity ratios histogram rates the probability of a single photon hit to create a given intensity ratio value.

In Fig. 1 an example of normalized intensity ratio histogram is plotted. The figure shows data computed for Au L photons from the measurement of Au bar pattern presented further in Section 3. As can be seen most of the photon hits create electron clouds with the intensity ratio in proximity to
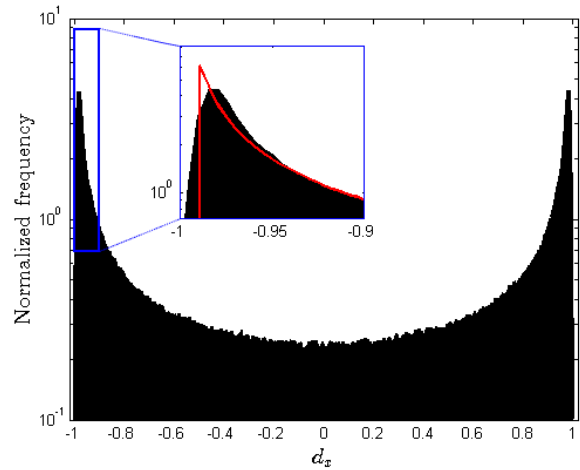

Fig. 1 An example intensity ratio histogram of Au L photons generated from a real measurement (Au bar pattern) with formula (6). The histogram is normalized to occupy a unitary area and can be identified with the probability density function. In the inset the histogram is compared to Gaussian simulation (red line).

−1 or 1. Intensity ratios close to 0 are the least probable. Discussed Gaussian model fits well to most values of the histogram; though for $|d_x| \approx 1$ (and $|d_y| \approx 1$) the simulation fails showing deficiency of the model.

2.3 Sub-pixel coordinates

Our method consist in converting the d_x and d_y intensity ratios of a given photon hit to x_0 and y_0 coordinates. In our approach we do not model the shape of the single photon electron cloud; we assume only separation of x and y components of the charge distribution. We also assume a uniform distribution of photon hits over the CCD plane. Accordingly the relation between the intensity ratio and single photon hit position is not simulated, but measured.

Lets set (x_i, y_j) – the pixel corner nearest to the point of a photon hit – to the origin, and the number of photon events to N. The possible values for x_0 inside a 2×2 pixel box span within $\left(-\frac{p}{2}, \frac{p}{2}\right)$, where p is the pixel dimension. Due to uniform distribution of photon hit positions over the CCD plane the probability of finding a photon hit with x coordinate below x_0 has a linear form:

$$P_x(x_0) = \frac{n(x\colon x < x_0)}{N} = \frac{x_0}{p} + \frac{1}{2}; \qquad (8)$$

here $n()$ stands for the number of elements of a set. We can also compute cumulative probability functions of d_x and d_y:

$$P_{d_x}(d_x) = \frac{n\left(\tilde{d}_x\colon \tilde{d}_x < d_x\right)}{N}, \qquad (9)$$

$$P_{d_y}(d_y) = \frac{n\left(\tilde{d}_y\colon \tilde{d}_y < d_y\right)}{N}. \qquad (10)$$

$P_{d_x}(d_x)$ and $P_{d_x}(d_x)$ are equivalent to normalized cumulative histograms of the measured intensity ratios.

If we note that d_x is monotonically increasing with x_0 then we get:

$$n\left(\tilde{d}_x\colon \tilde{d}_x < d_x(x_0)\right) = n\left(x\colon x < x_0\right). \qquad (11)$$

This directly shows that P_{d_x} can be identified with P_x:

$$P_{d_x}(d_x(x_0)) = P_x(x_0). \qquad (12)$$

Finally an explicit relation for x_0 can be given:

$$x_0 = p\left(P_{d_x}(d_x) - \frac{1}{2}\right). \qquad (13)$$

An analogical relation is also valid for y_0 and d_y.

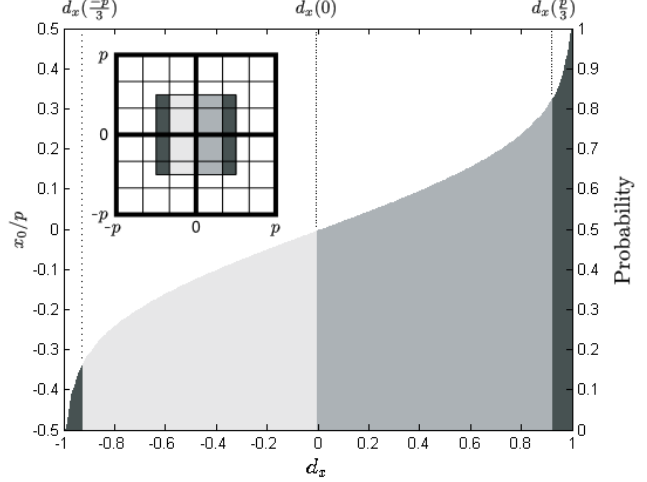The relationship between x_0, d_x and P_{d_x} is shown in Fig. 2.

Fig. 2 Relative photon hit position x_0 calculated as a function of intensity ratio d_x according to equation (13). Likewise in Fig. 1 the data for Au L photons from Au bar pattern are illustrated. Secondary vertical axis shows cumulative probability distribution P_{d_x}. In the inset a 2×2 pixel box with 3×3 sub-pixel division is shown. Different levels of gray mark – in order from darkest to brightest – central, left and right sub-pixels.

2.4 Division to sub-pixels

A strong point of our approach is that it requires only a good statistics of single photon hits ensuring high enough number of events N to minimize the statistic error of generated P_{d_x} and P_{d_y}. In particular the method is independent from the shape and creation process of the electron cloud and can deal with any, also asymmetric,[9] charge distributions. The cloud creation process and the resulting charge distribution is a characteristics of a given CCD and should not change in time. Therefore each measurement could be analyzed with the use of the same, previously obtained pixel intensity ratio probabilities.

In an ideal case of uniformly shaped electron clouds and a hypothetical noise-free CCD, equation (13) should give a strict position of a single photon hit. In reality the electron cloud is shaped randomly and the intensity signal from each pixel is given with an error. These two factors contradict the assumptions on monotonic relation between d_x and x_0 and on separation of x and y components. As a result the accuracy of sub-pixel coordinates is limited.

We can estimate an error on $d(I_1, I_2)$ with the following relation:

$$\delta d(I_1, I_2) = \frac{2\delta I \sqrt{I_1{}^2 + I_2{}^2}}{(I_1 + I_2)^2}, \qquad (14)$$

where δI is an error on a charge gathered in I_1 or I_2. Note that $\delta d(I_1, I_2)$ has its maximum for $I_1 = 0$ or $I_2 = 0$ which corresponds to $|d(I_1, I_2)| = 1$ or $|x_0| = \frac{p}{2}$. This is exactly where P_{d_x} exhibits the largest increase and, respectively, where the

error on P_{d_x} is the biggest.

As a result the photon hit position is most inaccurate in proximity to the pixel center $|x_0| = \frac{p}{2}$. In order to minimize that effect the sub-pixel division should comprise that higher uncertainty central region in a single sub-pixel. An exemplary division to 3 sub-pixels in x direction is shown in Fig. 2.

In conclusion, the assignment of sub-pixel coordinates to a given photon event consist only of two steps: (i) calculation of d_x and d_y with formulas (6) and (7), and (ii) comparison of obtained values with sub-pixel borders expressed in pixel ratio coordinates. As a result the algorithm is fast and can be applied on-line.

3 Experimental

To examine the performance of the sub-pixel algorithm two test samples were measured. The first one contains several microns of Au on a Si support arranged in bar-like patterns and a uniform reference layer.[20] The bar pattern consists of 10 Au lines with the width and the spacing between them decreasing from 10 μm to 1 μm in a 1 μm steps. The resolution limit can be easily found as the width of the narrowest recognizable line. The second structure was produced by the Fraunhofer-Institut für Zuverlässigkeit und Mikrointegration (IZM) in Berlin and consists of 3 μm thick and 30 μm wide Cu stripes deposited on Si wafer with 200 nm TiW adhesion layer. The stripes are aligned in parallel and distributed in groups with constant spacing of 30, 50 and 90 μm. Sketches of both structures are illustrated in Fig. 3.

Imaging was performed with two types of polycapillary lenses – a high-resolution conical optics with a 8:1 magnifi-

cation that was employed for the Au pattern, and a parallel 1:1 optics used for the Cu stripes structure. The magnification optics has a single channel entrance diameter of $d_{in} = 2\ \mu$m. The exit diameter of a channel span to $d_{out} = 16\ \mu$m which is one third of the pixel size ($p = 48\ \mu$m). A single channel diameter of the 1:1 optics amounts to $d = 24\ \mu$m which is half of the pixel size.

In order to ensure high enough photon count rate, measurements were performed at synchrotron radiation facility with the beam provided by the BAM*line* at BESSY II,[21] and at newly developed PIXE beam line (HS-PIXE) at Ion Beam Center at Helmholtz-Zentrum Dresden-Rossendorf (HZDR).[22] Detailed descriptions of two setups can be found in Ref. 3 and 22.

For imaging purpose Au L and Cu K lines intensity distributions were assessed. Valid photon events were selected with an algorithm described elsewhere.[3] The algorithm rejects the noise such as cosmic rays and accepts only photon events having an appropriate arrangement of pixels above the noise threshold.

The position of the photon hit is first estimated by the weighted position of the pixel with the highest intensity and its nearest neighbors. Subsequently a 2×2 pixel box around a pixel corner closest to the estimated position is selected and the sub-pixel algorithm is applied. The probability functions of pixel intensity ratios in x and y directions were obtained directly from the measurements. Probability density and cumulative probability functions of the intensity ratios in x direction for Au L photons are presented in Fig. 1 and 2.

4 Results

4.1 Au bar patter

In Fig. 4 the image of Au bar pattern is presented in normal resolution and with pixels divided to 2×2 and 3×3 sub-pixels. The normal resolution image exhibits strong pixelation introducing artificial jerking of the Au bars and decreasing the contrast between structure and background. Only the 4 thickest stripes can be distinguished in the original image; the rest is blurred. With the division into 2×2 sub-pixel another Au line is resolved. The 3×3 subpixel division, however, does not introduce any visible improvement. In this regime a single sub-pixel correspond to 2 μm distance on the sample which is exactly the entrance channel diameter of the polycapillary optics (2 μm). In addition the small effective area of a sub-pixel significantly lowers the count rate and increases the noise contribution.

In Fig. 5 three intensity profiles along a single (sub-)pixel row spanning along the whole Au bar structure are depicted. A profile intensity drop with pixel division is clearly visible. This is an effect of the sub-pixel area decrease. For a
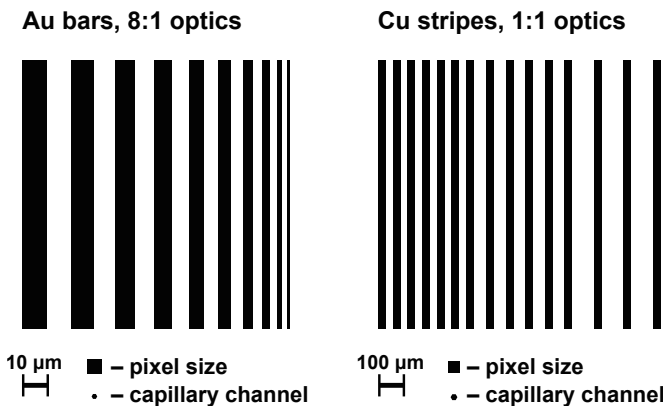
Au bars, 8:1 optics

Cu stripes, 1:1 optics

10 μm ■ – pixel size
• – capillary channel

100 μm ■ – pixel size
• – capillary channel

Fig. 3 Sketch of Au bar pattern (left) and Cu stripes (right). Structures were measured with, respectively, focusing 8:1 and parallel 1:1 optics; sizes of corresponding pixels (side length of, respectively, 6 μm and 48 μm) and capillary channels (entrance diameter of, respectively, 2 μm and 24 μm) are shown for comparison.
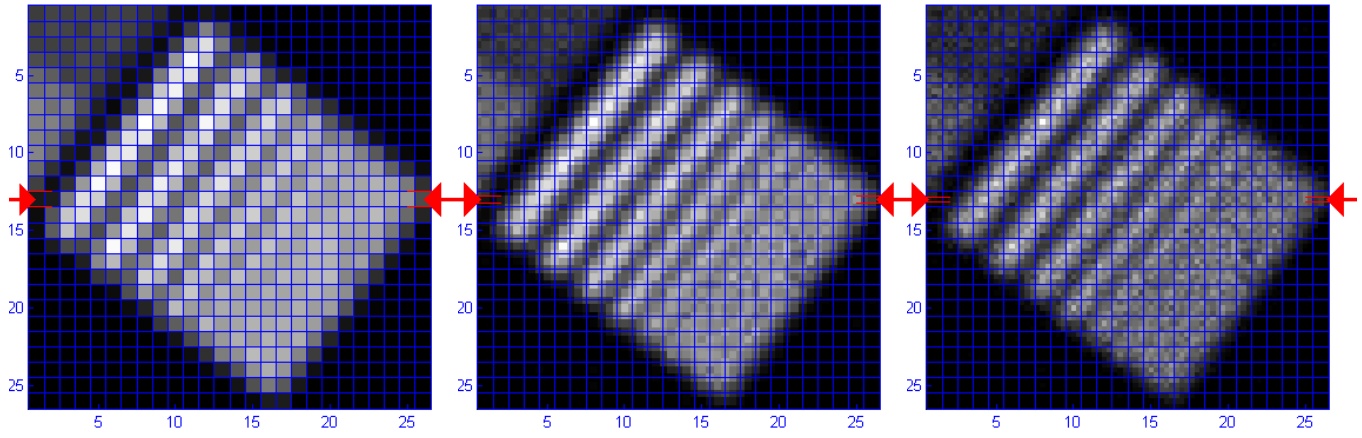
Fig. 4 Normal resolution (left), 2×2 (center) and 3×3 (right) sub-pixel division images of the Au bar pattern. The image was acquired at the BAM*line* at BESSY II with an 8:1 magnification lens. The grid shows the positions of the real pixels, each corresponding to $6 \times 6 \ \mu m^2$ area on the sample surface. Red flashes indicate the (sub-)pixel row chosen for comparison in Fig. 5.
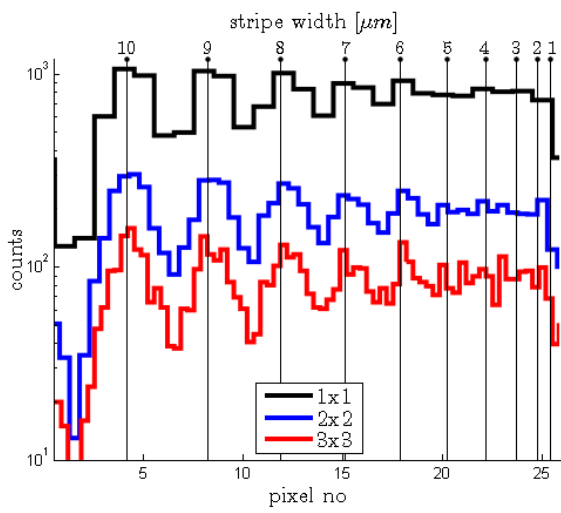

Fig. 5 Pixel intensity profiles along one sub-pixel row indicated in Fig. 4 with red rims. The profiles are plotted for normal resolution (black line), 2×2 (blue line), and 3×3 (red line) sub-pixel division. Estimated positions of the Au bar centers are indicated with black vertical lines. On top the actual Au stripe widths are given.
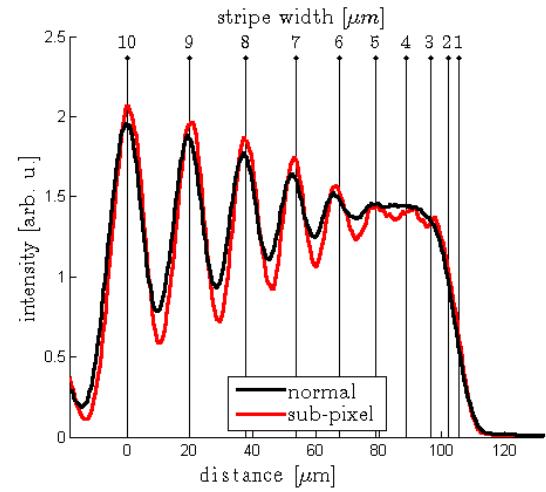

Fig. 6 Intensity profile across Au bar structures calculated for normal resolution (black line) and 3×3 sub-pixel division (red line) images. Estimated positions of the Au bar centers are indicated with black vertical lines. The intensity profile was constructed from data sampled at regular intervals across the Au bars. To increase the signal to noise ratio the intensity was integrated over the whole length of Au bars.

pixel divided to $n \times n$ sub-pixels the intensity is decreased n^2 times. However, the increased sampling frequency evidently increases the contrast. For the profile with no sub-pixel division only the 4 thickest Au bars can be definitely differentiated. The intensity valley between 6 μm and 5 μm bars is not visible. In case of 2×2 pixel division the 6 μm bar can be clearly distinguished. For 3×3 sub-pixel division, due to the considerable noise content, there is no significant amendment.

It should be noted that due to the Nyquist-Shannon sampling theorem,[6] details smaller than twice the sampling distance cannot be correctly distinguished. The theorem says that making n samples over a certain distance only a signal comprising less than $n/2$ elements can be rendered properly. Higher number of elements will lead to signal aliasing resulting in distortions and artifacts. Of course, with the sub-pixel division, this constrain is relaxed.

As a single pixel in a 8:1 magnified image represents a square with a side length of 6 μm the camera in standard resolution cannot correctly represent features smaller than 12 μm. Still, as can be seen in the presented example, even without sub-pixel resolution much smaller lines can be distinguished; though with some alterations. For instance in Fig. 5 the normal resolution profile shows the 8 μm bar to be thicker than the 9 μm one.

In Fig. 6 two additional intensity profiles are shown. The profiles represent the cumulative intensity across the lines parallel to Au bars sampled at regular intervals. The sampling interval was identical for both curves corresponding to normal resolution and 3×3 sub-pixel division; therefore the relative intensity of two profiles does not differ. For the sake of legibility the profile corresponding to 2×2 sub-pixel division is not present.

The tilt of the Au bar structure with respect to the pixel lines eliminates the effects due to pixelation. As a consequence the 6 μm Au bar can be resolved even in case of normal resolution. Also here the contrast improves when sub-pixel resolution is applied. In addition the enlarged integration area increases the statistics leveling the noise contribution. As a result the sub-pixel resolution profile allows distinction of 5 μm or even 4 μm bars.

4.2 Cu stripes

The consequences of too sparse sampling are clearly visible in the image of Cu stripes (see Fig. 7). The image represents a structure with three groups of Cu stripes with dimensions below the Nyquist-Shannon resolution limit. Here the structure is aligned with the pixels and the effect of aliasing is clearly visible. Normal resolution and 3×3 sub-pixel division images are presented for comparison.

The left most group is too confined and individual stripes cannot be distinguished even when sub-pixel resolution is ap-
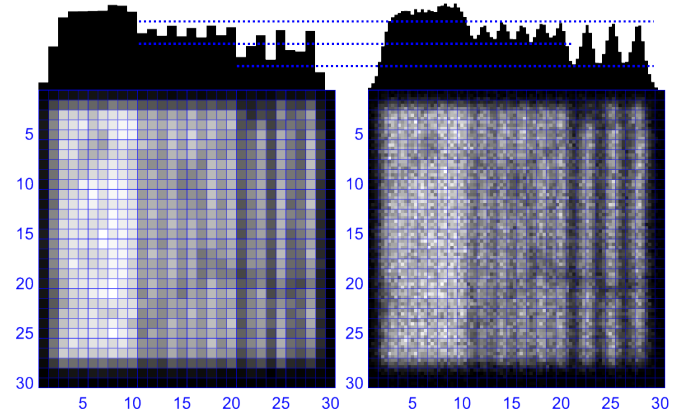

Fig. 7 Normal resolution (left) and 3×3 sub-pixel resolution (right) images of the Cu stripes pattern. The image was acquired at HS-PIXE beam line at HZDR with a parallel 1:1 optics. The grid shows the positions of the real pixels, each corresponding to 48×48 μm^2 area on the sample surface. On top the cumulative intensity along each (sub-)pixel column is presented. The dotted guide lines indicate the contrast levels for the sub-pixel resolution image.

plied. The structure has stripes with dimensions and spacing of 30 μm which is too close to the single capillary channel diameter (24 μm).

The stripes in the central group are distributed with interval of 90 μm, which is comparable to the Nyquist–Shannon resolution limit, *i.e.*, double the pixel size ($p = 48$ μm). In the standard image the stripes are merely distinguishable and confined to a single pixel line. The sub-pixel resolution image shows a much better representation of the structure.

Finally, the group on the right has an interval large enough to fulfill the Nyquist-Shannon theorem, but individual stripes are still below the limit. Therefore the structure is clearly resolved, however the stripe's widths and positions are not rendered well giving a false impression of a patchy structure. The sub-pixel resolution image correctly presents uniform, equidistant stripes.

For both central and right most group of stripes there is a noticeable increase of the contrast level when sub-pixel resolution is used. However, the contrast of the central group is much smaller. This is not surprising as the dimensions in the central group are much closer to the size of a single polycapillary channel which is an ultimate resolution limit.

4.3 Au layer

In order to test the limits of sub-pixel resolution algorithm an additional assay was performed on a reference Au layer. A small portion of the image was compared for the case of normal pixel resolution and increasing sub-pixel division (see Fig. 8). As can be seen very dense divisions lead to creation
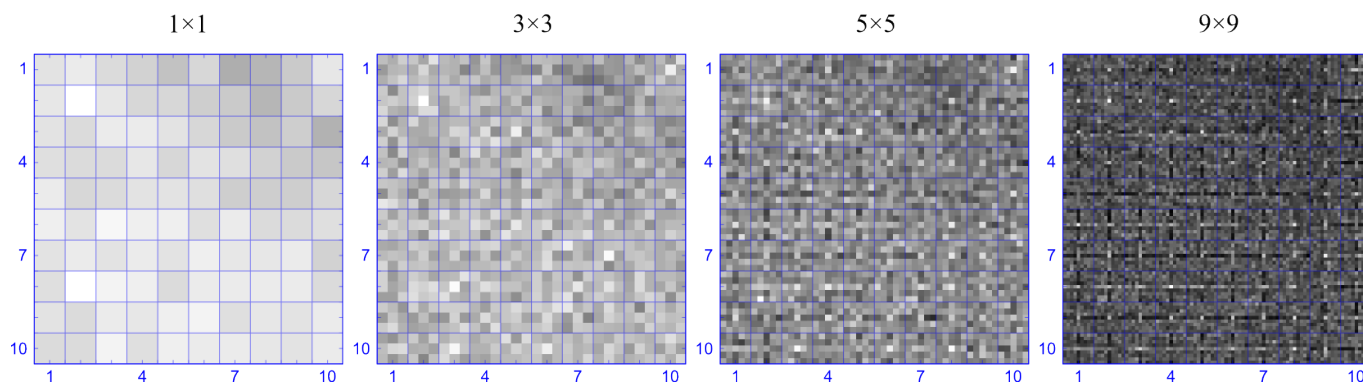
Fig. 8 Normal resolution and 3×3, 5×5, and 9×9 sub-pixel division images of a Au layer. The image was acquired at the BAM*line* at BESSY II with a 8:1 magnification lens. Artificial intensity structure following the pixel center position is strongly indicated for the sub-pixel resolution image. The grid shows the real pixel positions.

of intensity artifacts following the pixel center positions.

This effect was already discussed in Section 2.4 and is a result of the uncertainty of a position of a photon hit reaching the middle area of a pixel. Nevertheless, pixel divisions up to 5×5 sub-pixels are usually not so much affected by this inconvenience. It should be noted that due to a nonzero divergence of transmitted photons and a nonzero optics-detector distance in SLcam® the footprint of a single polycapillary channel on the detector cannot decrease below a dozen of microns. Thus, keeping in mind that the dimension of a pnCCD pixel is 48 μm, a pixel division into 5×5 sub-pixels should be sufficient to reach the optimal limits of resolution.

5 Summary

We propose a modified approach to sub-pixel resolution algorithm taking into account all the photon events occurring on a CCD plane. The sub-pixel position of the photon hit is assessed from the pixel footprint of the generated electron cloud. The calculations are performed based on the pixel intensity ratios of a 2×2 pixel box holding photo electrons. The method is independent from the actual shape and creation process of the charge cloud and does not reject the photon events from the pixel center. The algorithm is fast and can be employed on-line.

The sub-pixel resolution was applied to several test structures. A notable enhancement in quality of the acquired images comprising contrast and resolution improvement, as well as elimination of aliasing due to pixelation was demonstrated. For images acquired with 8:1 magnifying optics a resolution limit of 5 μm was assessed. Due to an electronic noise and random variations of electron cloud shape the sub-pixel coordinates cannot be given with unlimited precision. It was shown that in case of 48×48 μm^2 pixel pnCCD the 5×5 sub-

pixel division is a realistic limit of the method.

References

1 A. Kühn, O. Scharf, I. Ordavo, H. Riesemeier, U. Reinholz, M. Radtke, A. Berger, M. Ostermann and U. Panne, *J. Anal. At. Spectrom.*, 2011, **26**, 1986–1989.

2 I. Ordavo, S. Ihle, V. Arkadiev, O. Scharf, H. Soltau, A. Bjeoumikhov, S. Bjeoumikhova, G. Buzanich, R. Gubzhokov, A. Günther, R. Hartmann, P. Holl, N. Kimmel, M. Kühbacher, M. Lang, N. Langhoff, A. Liebel, M. Radtke, U. Reinholz, H. Riesemeier, G. Schaller, F. Schopper, L. Strüder, C. Thamm and R. Wedell, *Nucl. Instrum. Methods Phys. Res., Sect. A*, 2011, **654**, 250 – 257.

3 O. Scharf, S. Ihle, I. Ordavo, V. Arkadiev, A. Bjeoumikhov, S. Bjeoumikhova, G. Buzanich, R. Gubzhokov, A. Günther, R. Hartmann, M. Kühbacher, M. Lang, N. Langhoff, A. Liebel, M. Radtke, U. Reinholz, H. Riesemeier, H. Soltau, L. Strüder, A. F. Thünemann and R. Wedell, *Anal. Chem.*, 2011, **83**, 2532–2538.

4 L. Strüder, U. Briel, K. Dennerl, R. Hartmann, E. Kendziorra, N. Meidinger, E. Pfeffermann, C. Reppin, B. Aschenbach, W. Bornemann, H. Bräuninger, W. Burkert, M. Elender, M. Freyberg, F. Haberl, G. Hartner, F. Heuschmann, H. Hippmann, E. Kastelic, S. Kemmer, G. Kettenring, W. Kink, N. Krause, S. Müller, A. Op-

pitz, W. Pietsch, M. Popp, P. Predehl, A. Read, K. H. Stephan, D. Stötter, J. Trümper, P. Holl, J. Kemmer, H. Soltau, R. Stötter, U. Weber, U. Weichert, C. von Zanthier, D. Carathanassis, G. Lutz, R. H. Richter, P. Solc, H. Böttcher, M. Kuster, R. Staubert, A. Abbey, A. Holland, M. Turner, M. Balasini, G. F. Bignami, N. L. Palombara, G. Villa, W. Buttler, F. Gianini, R. Lainé, D. Lumb and P. Dhez., *Astron. Astrophys.*, 2001, **365**, 18–26.

5 A. Bjeoumikhov, N. Langhoff, R. Wedell, V. Beloglazov, N. Lebed'ev and N. Skibina, *X-Ray Spectrom.*, 2003, **32**, 172–178.

6 C. E. Shannon, *Proceedings of the IRE*, 1949, **37**, 10–21.

7 H. Tsunemi, K. Yoshita and S. Kitamoto, *Jpn. J. Appl. Phys.*, 1997, **36**, 2906–2911.

8 M. Pivovaroff, S. Jones, M. Bautz, S. Kissel, G. Prigozhin, G. Ricker, H. Tsunemi and E. Miyata, *IEEE Transactions on Nuclear Science*, 1998, **45**, 164–175.

9 H. Tsunemi, J. Hiraga, K. Yoshita and E. Miyata, *Jpn. J. Appl. Phys.*, 1999, **38**, 2953–2957.

10 K. Yoshita, H. Tsunemi, E. Miyata, K. Gendreau and M. Bautz, *IEEE Transactions on Nuclear Science*, 1999, **46**, 100–106.

11 J. Hiraga, H. Tsunemi and E. Miyata, *Jpn. J. Appl. Phys.*, 2001, **40**, 1493–1498.

12 J. Li, J. H. Kastner, G. Y. Prigozhin and N. S. Schulz, *The Astrophysical Journal*, 2003, **590**, 586–592.

13 N. Kimmel, J. S. Hiraga, R. Hartmann, N. Meidinger and L. Strüder, *Nuclear Instruments and Methods in Physics Research Section A: Accelerators, Spectrometers, Detectors and Associated Equipment*, 2006, **568**, 128 – 133.

14 A. Abboud, S. Send, N. Pashniak, W. Leitenberger, S. Ihle, M. Huth, R. Hartmann, L. Strüder and U. Pietsch, *Journal of Instrumentation*, 2013, **8**, P05005.

15 F. Scholze, H. Rabus and G. Ulm, *Journal of Applied Physics*, 1998, **84**, 2926–2939.

16 J. R. Janesick, *Scientific Charge-Coupled Devices (SPIE Press Monograph Vol. PM83)*, SPIE Publications, 2001.

17 G. R. Hopkinson, *Optical engineering*, 1987, **26**, 268766–268766.

18 E. Miyata, M. Miki, D. Kamiyama, H. Tsunemi and K. Miyaguchi, *Jpn. J. Appl. Phys.*, 2003, **42**, 7135–7139.

19 D. Lawrence, P. O'Connor, J. Frank and P. Takacs, *Publications of the Astronomical Society of the Pacific*, 2011, **123**, 1100–1106.

20 E. Strub, M. Radtke, U. Reinholz, H. Riesemeier and E. Reznikova, *Nuclear Instruments and Methods in Physics Research Section B: Beam Interactions with Materials and Atoms*, 2008, **266**, 2165 – 2168.

21 H. Riesemeier, K. Ecker, W. Görner, B. Müller, M. Radtke and M. Krumrey, *X-Ray Spectrom.*, 2005, **34**, 160–163.

22 S. H. Nowak, A. Bjeoumikhov, J. von Borany, J. Buchriegler, F. Munnik, M. Petric, A. D. Renno, M. Radtke, U. Reinholz, O. Scharf, L. Strüder, R. Wedell and R. Ziegenrücker, *X-Ray Spectrom.*, DOI 10.1002/xrs.2590.